EXAFS spectroscopy as a tool to probe metal–support interaction and surface molecular structures in oxide-supported catalysts: application to Al2O3-supported Ni(ii) complexes and ZrO2-supported tungstates

Xavier Carrier, Eric Marceau, Hugo Carabineiro, Vicente Rodríguez-González, Michel Che

HAL Id: hal-01496028

https://hal.sorbonne-universite.fr/hal-01496028v1

Submitted on 27 Mar 2017

EXAFS spectroscopy as a tool to probe metal-support interaction and surface molecular structure in oxide-supported catalysts: application to Al$_2$O$_3$-supported Ni(II) complexes and ZrO$_2$-supported tungstates

Xavier Carrier,[1,2,*] Eric Marceau,[1,2] Hugo Carabineiro,[1,2,3,#] Vicente Rodríguez-González[1,2] and Michel Che[1,2,4]

[1] UPMC - Université Pierre et Marie Curie (Paris 06), Laboratoire de Réactivité de Surface, UMR 7197, F-75005, Paris, France

[2] CNRS, Laboratoire de Réactivité de Surface, UMR 7197, F-75005, Paris, France

[3] Centro de Engenharia Biológica e Química, Instituto Superior Técnico, Universidade Técnica de Lisboa, Avenida Rovisco Pais, 1049-001 Lisboa, Portugal

[4] Institut Universitaire de France

[*] To whom correspondence should be addressed. Phone: 33 1 44 27 60 05. Fax: 33 1 44 27 60 33. E-mail address: xavier.carrier@upmc.fr

[#] present address: UOP Ltd

Figures: 7

Tables: 3

SUMMARY

EXAFS spectroscopy is shown as a tool of prime importance to probe the formation of metal-oxygen-support bonds and unravel the surface molecular structure in oxide-supported systems through two examples: i) a molecular metal complex (Ni(II) bisglycinate) characterized after impregnation and drying on Al_2O_3, and ii) a tungsten oxide nanophase characterized after deposition on zirconia and high temperature thermal treatment (tungstated zirconia catalysts, i.e. WO_x/ZrO_2). Unlike other spectroscopic techniques, EXAFS at the Ni K-edge proves that a modest thermal activation during the impregnation step triggers the grafting of nickel(II) bisglycinate onto the support: Al next-nearest neighbours are detected when the impregnation is carried out at 60°C instead of room temperature. Characterization of WO_x/ZrO_2 catalysts shows the presence of W next-nearest neighbours around tungsten, with W-W distances distinctive of edge-shared WO_6 octahedra only. The WO_x overlayer can thus be described as bidimensional, nanometric slabs of 4 to 5 WO_6 units on each side. In these slabs, W octahedra are interconnected to form a more condensed structure than the one present in bulk WO_3 (in which linkage through corners exists). Moreover, EXAFS results conclusively demonstrate that the WO_x overlayer is directly anchored to the ZrO_2 surface by means of W-O-Zr bonds with a W-Zr distance of 3.14 Å.

KEYWORDS: Heterogeneous catalysts, catalyst preparation, XAS, tungstated zirconia, Ni-based catalysts, zirconia, alumina.

INTRODUCTION

A molecular-level approach of the surface structure of heterogeneous oxide-supported catalysts is a definite pre-requisite for a proper understanding and ultimately improvement of catalyst performances (activity, selectivity and stability).[1] However, heterogeneous metal-oxide catalysts are made of nanometer-sized oxide particles dispersed on an inorganic support (alumina, silica, carbon…) that inherently lack long-range order, which prevents the use of crystallographic techniques for their characterization. The situation is even more critical for supported complexes or polyanions, because the deposited species are molecularly distributed on the surface. One thus has to rely on a combination of surface spectroscopic methods to establish the molecular structure of these entities and determine which parameter from the preparation procedure would lead to the most effective interaction with the support.[2-4] Unfortunately, most characterization techniques either give a partial picture of the surface structure, or appear to be silent if the creation of metal-oxygen-support bonds does not significantly perturb the first coordination sphere of the metal.[5] As an example, Raman spectroscopy allows one to differentiate between mono-oxo and di-oxo surface species,[6] and polymeric *vs*. monomeric species. But this technique is much less convincing when the symmetry is concerned (octahedral *vs*. tetrahedral) and nearly blind with respect to metal-oxygen-support bonds, even in the simplest case, *i.e.* highly dispersed mononuclear species.[7] A topical example is the surface structure of group 6 elements on silica, for which surface species with terminal mono-oxo[6, 8] di-oxo bonds[9, 10] or a mixture of both[11] have been suggested. In these systems, the existence and number of metal-support bonds (*i.e.*, Mo-O-Si) are conjectured on the basis of Lewis structures (tetrahedral di-oxo species with two metal-support bonds ("SiO_2MoO_2") or pentahedral mono-oxo species with four metal-support bonds ("SiO_4MoO")) but never spectroscopically demonstrated, while it is a key information to assess the dispersion and reactivity of the active phase in supported catalysts.

One of the most interesting spectroscopic techniques able to unravel the formation of metal-oxygen-support bonds and surface structure in supported catalysts is X-ray Absorption Spectroscopy (XAS).[12, 13] Contrarily to X-ray diffraction, XAS is not conditioned by the existence of a long-range order and since it involves X-ray photons, it can be performed under reaction conditions. As a consequence, it has been widely used in the field of heterogeneous catalysis to assess the molecular structure of the active phase.[3, 14] In particular, the study of the Extended X-ray Absorption Fine Structure (EXAFS) provides information on the local environment around a specific atom, including the second coordination sphere. It also allows one a quantitative description regarding the number of neighbours, their distance from the element studied as well as an assessment of the structural and thermal disorder.[15]

However, there are only few reports where EXAFS could demonstrate the existence of metal-oxygen-support bonds (i.e. M-O-S) in a system supported on a non-organized oxide,[3, 16-18] probably for at least two reasons: i) metal-support bonds may have different lengths and ii) the support constituents are frequently low Z elements (*e.g.* Al, Si…). These two aspects lead to large Debye-Waller factors (structural disorder) as well as weak backscattering amplitudes in the EXAFS signal (low Z scatterers), and thus weak contributions to the overall signal. Previous EXAFS works giving conclusive indications on the formation of M-O-S bonds, can be classified in two main categories: i) supported molecular compounds highly dispersed on oxide supports and ii) surface precipitate formed from dissolution or destruction of the support.

In the first category, EXAFS was used to confirm that molecular precursors or catalytically active species are chemically grafted onto a support which have led to important conclusions in recent years. One can note the following examples:

- By determining the number of silicon next-nearest neighbours around Ni^{2+}-ethylenediamine complexes (from 1 to 3), Boujday et al.[16] were able to show that specific sites of amorphous

silica stabilize grafted complexes depending on the number of labile positions in the coordination sphere of nickel, leading to a supramolecular approach of interfacial coordination chemistry.

- In supported organometallic catalysis, EXAFS is used to probe the grafting of molecular complexes onto a silica, alumina or zirconium hydroxide surface[19, 20] and to determine the geometry of the adsorption site around the active species (for example, a siloxane bridge close to a tungsten atom[21]).

- Interactions between methytrioxorhenium species and Al Lewis sites of silica-aluminas (Al next-nearest neighbour detected at 3.06 Å) may account for the activity of the supported species in olefin metathesis, while the unsupported precursor is not active.[22]

- By detecting one Si, Al or Nb next-nearest neighbour between 2.6 and 3.1 Å, the existence of a single bond between the support and vanadate species used in selective oxidation is confirmed.[23]

- The existence of very small gold clusters (4-6 atoms) on Au/MgO catalysts prepared from dimethylgold complexes and used in CO oxidation is consistent with the addition of Mg next-nearest neighbours to Au to complete a satisfactory fitting of the EXAFS signal.[24]

The second category concerns the extensive literature data demonstrating the formation of surface precipitates (mixed neophase) from oxide support dissolution and subsequent reaction of dissolved species with metal precursors. Specifically, it has been shown that contacting an oxide support (alumina and silica for example) with a metal salt solution (i.e. Co(II) or Ni(II)) may lead to the surface precipitation of clay-type mixed neophases such as phyllosilicate[25-27] or hydrotalcite (layered double hydroxide).[28, 29] These surface precipitates, containing both types of ion from the support and metal precursors, lead to the existence of an extensive network of M-O-S bonds. However, identification of such bonds with EXAFS spectroscopy is not an easy task too since the Radial Distribution Function (RDF) for phyllosilicates and

hydrotalcites is very similar to that of the parent hydroxides ($Ni(OH)_2$ or $Co(OH)_2$) having metal-oxygen-metal (M-O-M) bonds only. As a matter of fact, clay-type neophases and pure hydroxides have similar M-O-M distances while the weak backscattering amplitude of Al or Si relative to Co or Ni for example does not allow one to give any conclusive evidence from fitting procedures only. However, it has been shown that the existence of Ni(Co)-O-Si(Al) bonds in phyllosilicate-like or hydrotalcite-like surface phases can be decisively established by careful examination of the EXAFS spectrum in the R space (between 3 and 5 Å)[30] or in the k-space (presence of a characteristic beat pattern at 8 Å^{-1}).[31] Similar observations have also been made on catalysts prepared by solid state reactions.[32, 33]

In this contribution, we would like to demonstrate, from two selected examples (alumina-supported Ni(II) complexes and tungstated zirconia), that the use of EXAFS is worthwhile if one wants to propose a comprehensive molecular-scale description of metal-oxygen-support interactions for systems that resist analysis by conventional spectroscopic methods. In the first example, the identification of a preparation parameter promoting the complexes grafting onto the support surface will be identified. In the second example, an unusual surface compound will be characterized and its stabilization by the zirconia support evidenced.

EXPERIMENTAL

1. X-ray absorption spectroscopy. XAS data were collected at the Laboratoire pour l'Utilisation du Rayonnement Electromagnétique (LURE - France) on beamline D42 and D44 using channel-cut Si (111) crystals. The electron energy and ring current were 1.85 GeV and 250 mA, respectively. Ni K-edge (8333 eV) and W L_{III}-edge (10204 eV) spectra were recorded in the transmission mode in air, at room temperature and 77K respectively, with ion chambers detectors. Calibration of the monochromator was performed with Ni and W-metal foils. The energy was scanned with incremental energy steps of 2 eV/point from 8250 to 9200 eV at the Ni K-edge, and 2 eV/point from 10,100 to 10,200 eV, 1 eV/point from 10,200 to 10,350 eV and 2 eV/point from 10,350 to 11,000 eV at the W L_{III}-edge. The samples were thoroughly ground, mixed with cellulose and pressed in the form of pellets. A total of 3 to 4 scans were collected for each sample for an analysis time of about 2 hours.

EXAFS data extraction was performed by standard procedures[15] using Michalowicz's software package.[34] Fourier Transforms (FT) of $w(k)\, k^3\, \chi(k)$ EXAFS data ($w(k)$ is a Kaiser-Bessel window with a smoothness parameter of 3.0 or 2.5 for the W and Ni edges respectively) were then carried out in the 2.2-11.8 Å^{-1} range (Ni edge) and 2.3-14.0 Å^{-1} range (W edge) in order to obtain a radial distribution function (RDF). Each coordination shell of the RDF was then filtered using inverse Fourier transformation and k^1-weighted Fourier filtered data were fitted in the k-space. Fourier transformation and Fourier filtering were conducted using "EXAFS98" and multiple shell fitting was carried out with "Round Midnight".[34] Experimental phase-shifts and amplitudes were obtained from reference compounds. The W-O parameters were extracted from the first oxygen shell in Na_2WO_4 (Aldrich), while W-W parameters were obtained from the second shell of tetrabutylammonium hexatungstate ($[N(C_4H_9)_4]_2[W_6O_{19}]$).[35] Experimental phases and

amplitudes were preferred since these include the multi-body S_0^2 term and the mean free path dependence on energy. However, theoretical phase and amplitude parameters for the W-Zr pair had to be theoretically calculated using the FEFF8 code.[36] Debye-Waller factors, which account for structural and thermal disorder, are referred to the experimental reference ($\Delta\sigma$) except for W-Zr where it must be taken as an absolute value. Moreover a S_0^2 value of 0.9 was considered to correct the coordination number only for the W-Zr shell. Similarly, the Ni-O, Ni-N and Ni-C parameters were extracted from experimental data recorded on $[Ni(H_2O)_6](NO_3)_2$ and $[Ni(en)_3](NO_3)_2$, while calculated functions were used for Ni-Al pairs, because of the lack of reference compounds.

The electron mean free path as well as the multi-body term were integrated in the amplitude function extracted from experimental references. The quality of the fit was evaluated through the agreement factor (Eq. 1):[34]

Eq. 1
$$R^2 = \frac{\sum_i \left(k\chi_{th}(k) - k\chi_{exp}(k)\right)^2}{\sum_i \left(k\chi_{exp}\right)^2}$$

2. Other characterization techniques

Elemental analyses were determined by inductively coupled plasma-atomic emission spectroscopy (ICP-AES, Service Central d'Analyse, CNRS, Vernaison, France). Specific surface areas were measured on a Micromeritics 2010 apparatus using multipoint N_2 physisorption isotherms at 77 K. Catalysts samples were activated at 423 K overnight in dynamic vacuum prior to nitrogen adsorption. Surface areas were calculated based on the Brunauer-Emmet-Teller (BET) equation in the $P/P_0 = 0.05$-0.30 range. X-Ray Diffraction (XRD) analyses were carried out on a Siemens D500 diffractometer, using Cu Kα radiation (1.5418 Å). UV-Visible-Near Infrared (UV-Vis-NIR) spectra were recorded with a resolution of 1 nm in the transmission mode on a Cary 5 spectrometer (Varian). UV-Vis-NIR spectra of

the solids were recorded in the reflectance mode (1 nm resolution) on the same spectrometer equipped with an integration sphere, using Teflon as a reference. Infrared (IR) spectra recorded on KBr pellets were collected with a FT-IR M-1700 Perkin-Elmer spectrometer with a 4 cm^{-1} resolution. Raman spectra were recorded on powders with a modular HL5R spectrometer equipped with a microscope (Kaiser Optical Systems, Inc.), a near-infrared laser diode working at 785 nm, a Charge Coupled Device detector providing fast collection of Raman data from 100 to 3450 cm^{-1} (average resolution 2 cm^{-1}) and holographic Notch filters.

RESULTS AND DISCUSSION

A. Al$_2$O$_3$-supported Ni(II) bisglycinate

A.1 Support-complexes interactions and heterogeneous catalysts

Grafting of complexes onto an oxidic surface are usually searched for in catalysis for two reasons: i) the complex is the catalytic active species (surface organometallic chemistry) and must be immobilized so as to avoid leaching and ensure the existence of single sites of defined geometry; ii) the complexes are the precursors of the active phase and their initial dispersion over the surface augurs well for the final dispersion of the phase obtained after thermal treatment.[37] Grafting usually occurs by substitution of hydroxyl groups of the surface to one or several labile ligands of the complexes and is often evidenced by shifts of absorption bands in the UV-Visible spectrum.[38, 39] However, the task is difficult when UV-Visible spectroscopy is silent (by lack of transitions or because no shift can be observed) and when no information on the ligands lability is known. In this example, we use EXAFS as a tool so as to identify under which conditions a stable model complex, *trans*-[Ni(glycinate)$_2$(H$_2$O)$_2$], expected to interact poorly with the support given its electrical neutrality, can become grafted onto an alumina surface.

A.2 Preparation

The *trans*-diaquabis(glycinato-O,N) Ni(II) complex ([Ni(glycinate)$_2$(H$_2$O)$_2$], hereafter referred to as nickel bisglycinate) was synthesized following the procedure described in Rodríguez-González et al.[40, 41] Initial dissolution of the complexes in water was carried out at 333 K, yielding 0.025 mol Ni.L^{-1} solutions. Two solutions were used for alumina impregnation: one was left to cool down to ambient temperature before impregnation (used to prepare sample NGamb), while the other one was kept at 333 K throughout the process of impregnation (used

to prepare sample NG333). The pH of the solutions was 7. One g of γ-alumina (EC1285, supplied by the Institut Français du Pétrole; specific surface area 200 $m^2.g^{-1}$, pore volume 0.52 $cm^3.g^{-1}$) was added to 10 mL of each solution and the suspensions were left under stirring for 15 min. Water was removed by evaporation at reduced pressure (0.1 bar) at 333 K. The solids were then dried at 353 K for 12 h and kept in a dessicator. The final content in nickel was 1.5 wt%. Elemental analyses carried out on the supported samples confirmed the initial stoichiometry of the complexes (N wt% = 0.7, N/Ni = 2). No change in the support characteristics (surface area, porosity) was observed.

A.3 Spectroscopic study

A.3a Conventional techniques. At first, samples NGamb and NG333, prepared at room temperature and at 333 K respectively, appear to be quite similar. It is difficult to reach firm conclusions on the Ni^{2+} ions environment from the UV-visible spectra (see electronic supplementary information). In each case, three absorption bands close to 380, 630 and 1030 nm are consistent with data recorded on the pseudo-octahedral, pristine complexes in their crystallized form but some bands shift to higher wavelengths while other shift to lower wavelenghts. Furthermore, no crystals of nickel bisglycinate are detected on alumina by X-ray diffraction. Actually, the amount of complexes is lower than a theoretical monolayer (1.5 Ni wt% compared to 3.5 Ni wt% for a monolayer, if one supposes that one complex occupies a circle of diameter 8.1 Å defined by the distance between the two external oxygens of the glycinate ligands).

The presence of crystals can also be discarded on the basis on infrared and near infrared data (see electronic supplementary information). For instance, bands assigned to CH_2 groups come out at 2940 and 2980 cm^{-1} ($\nu_s(CH)$ and $\nu_{as}(CH)$, IR) and 2270 nm (combination band $\nu+\delta(CH_2)$, NIR) for the crystallized complexes, while for the supported complexes, the

band ν_{as}(CH) at 2980 cm^{-1} and its overtone at 1690 nm (NIR) are barely visible, and the combination band is located at 2258 nm. Similar shifts are observed for the NIR bands attributed to the NH$_2$ groups: for crystals, overtone bands 2ν(NH) are observed at 1540 and 1553 nm, and the combination band at 2038 nm, compared with 1515, 1530 and 2020 nm for the supported complexes.

In the crystals, complexes are held together by a network of strong hydrogen bonds between the terminal aqua ligands (H-donors) and the two oxygen atoms from the coordinated –COO$^-$ groups (H-acceptors). Though the CH$_2$-NH$_2$ moieties do not participate directly in the intermolecular bonding, it can be supposed that the disruption of hydrogen bonding between complexes modifies the conformation of the ligands, leading to vibrations of higher energy when nickel bisglycinate is present as isolated species. But it is difficult to go further in the characterization of the two supported samples by conventional laboratory techniques and the assistance of X-ray absorption spectroscopy at the Ni K edge is required.

A.3b Grafting evidenced by EXAFS. Prior to the analysis of EXAFS data, scattering paths in [Ni(glycinate)$_2$(H$_2$O)$_2$] were identified by application of FEFF7 to the crystal structure of solid nickel bisglycinate. Indeed, multiple scattering involving Ni-C-O-Ni and Ni-C-N-Ni paths occur above 3.1 Å, which implies that an EXAFS simulation based on simple scattering can be carried out on the first two shells of neighbours only (Fig. 1, uncorrected for phase shift). Consequently, the external oxygens of the carboxyl groups and all the atoms beyond (for example atoms of other bisglycinate complexes in the crystals) will not be considered for fitting.

As Figure 1 shows, the Fourier transforms of the EXAFS signals recorded for the complexes in a 0.08 mol.L^{-1} solution, in crystals, on NGamb and on NG333 are identical as far as the nearest neighbours are concerned. The first shell can be fitted using O and N backscatterers, confirming that the pseudo-octahedral arrangement of ligands is not modified

upon deposition on alumina (Table 1, Fig. 2). Except for NG333, the second shell consists exclusively of four carbon atoms, in line with the stoichiometry of the complex. Disorder assessed through the Debye-Waller parameter is higher on NGamb than for the complexes in solution. In contrast, for NG333 the second shell exhibits two components (see the arrow on Fig. 1), indicating that other atoms can be detected in the vicinity of nickel. A good fit is obtained by keeping the four carbon atoms of the two glycinate ligands, responsible for the maximum of the peak, and adding aluminium atoms at R = 3.05 Å, to account for the component at higher distances. It is difficult to interpret the fractional value of N for Al toms, because the system is probably disordered and heterogeneous in terms of interactions between the complexes and alumina.

A.4 Probing support-complex interactions on alumina

This example shows that unlike other physicochemical techniques that lead to similar results (including UV-visible spectroscopy in this particular case), X-ray spectroscopy is sensitive enough to distinguish between systems which contain complexes grafted onto the support (for which Al next-nearest neighbours are detected) and systems in which the metal ion does not have direct bonding with the support surface. Since drying conditions were identical for the two samples, it is likely that for NG333, thermal activation during impregnation has favoured the replacement of an aqua ligand by a hydroxyl group of alumina. Moreover, interactions between the neutral complex and the weakly charged surface of alumina at pH 7 can be interpreted neither on the basis of grafting nor electrostatic interactions for NGamb. The only other possibility is the establishment of hydrogen bonds between the aqua and glycinate ligands on one hand, and the alumina hydrated surface on the other hand. New steric constraints would explain the changes in the infrared spectrum in terms of bands position and intensity (see the CH_2 group). By evidencing the existence of

metal-oxygen-support bonds in one case, EXAFS has allowed one to identify temperature as a key parameter to favour grafting of the neutral complexes during impregnation, and, indirectly, to help deduce which unusual type of interactions is probably involved in the deposition of nickel bisglycinate on alumina at room temperature.

B. Tungstated Zirconia.

B.1 Tungstated Zirconia in catalysis

Skeletal isomerization reactions of light alkanes (C_4-C_6) is of tremendous importance in the petroleum refining industry since it leads to high value products (isobutene used as fuel additive via the production of MTBE for example) or octane number enhancers. Tungstated zirconia catalysts (WO_x/ZrO_2) are interesting candidates for this reaction as alternative for environmentally harmful acid catalysts (liquid acids or halogenated aluminas).[42] WO_x/ZrO_2 catalysts were first believed to be superacid solids because they were able to activate light straight-chain alkanes like *n*-butane, which usually calls for very strong acid sites.[43] However, recent research progress has led to a gradual rejection of the existence of acid sites stronger than 100% sulphuric acid.[44] Alternatively, it was proposed the intervention of redox processes in the activation of alkanes[45] or in the genesis and maintenance of a temporary Brønsted acidity[46, 47] formed under reaction conditions upon reduction of WO_x domains of appropriate size. Despite the fact that there is no general consensus on this issue up to now, it seems well established that a maximum in the acidic catalytic activity is found for an optimal tungsten surface density corresponding more or less to a saturation coverage of the zirconia surface by WO_x domains.[44, 46, 48] The different literature reports converge to describe these domains as made up of a polytungstate overlayer formed by a three-dimensional network of linked WO_6 groups, in which W is in distorted octahedral environment coordinated to oxygen atoms.[47, 49-52] However, molecular-scale description of this tungsten overlayer is still lacking. In this

section, we use EXAFS spectroscopy in order to shed more light on these surface species and a plausible structural model is proposed.

B.2 Preparation

B.2a. Synthesis of zirconia. In order to circumvent the limitations imposed by the ubiquitous presence of Hf impurities in most of the commercial zirconia precursors and zirconium oxide (see B.3a), an Hf-free $ZrCl_4$ was used (Aldrich, Hf < 50 ppm) for the preparation of hydrous zirconia ($ZrO_x(OH)_{4-2x}$). The final Hf content in the WO_x/ZrO_2 catalysts was actually 30-40 ppm *vs.* about 0.5% wt. for catalysts obtained from commercial zirconium hydroxide. 70 g of $ZrCl_4$ were dissolved in 600 mL of distilled water to obtain a 0.5 mol.L^{-1} solution. A concentrated ammonia solution (15.7 N) was then added dropwise under vigorous stirring. The zirconium solution became gradually jellified as the pH increased until a final value of 7.4 was reached. The gel of ill-defined composition $ZrO_x(OH)_{4-2x}$ was then washed and centrifuged 7 times in distilled water until no Cl^- ions could be detected by addition of a drop of a 0.1 M $AgNO_3$ solution. For the sake of simplicity, the precipitate of zirconium hydroxide will be hereafter denoted as $ZrO_x(OH)_{4-2x}$.

B.2b. Catalyst preparation. The dried amorphous $ZrO_x(OH)_{4-2x}$ powder was then suspended in 150 mL of an aqueous solution of ammonium metatungstate (($NH_4)_6[W_{12}O_{40}H_2]$, Fluka) with the desired amount of W and refluxed for about 22 h. Water was evaporated; the powder dried overnight in an oven at 383 K for 12 h was subsequently calcined in a quartz reactor under 50 $cm^3\,min^{-1}$ of dry air for 3 h at 923 or 1098 K. The samples are labelled xWZ($ZrCl_4$)y, where x denotes the tungsten content on a WO_3 weight basis and y is the calcination temperature in Kelvin. The detailed results of surface area, elemental analysis, W surface density and tetragonal volumetric fraction[53] are given in Table 2 for each of the three samples.

B.3 Choice of the reagents and reference compounds

B.3a Effect of the presence of Hf impurities

Previous attempts to analyze EXAFS spectra recorded over tungstated zirconia catalysts have been seriously compromised by the ubiquitous presence of Hf impurities in zirconia.[50, 54, 55] Even for Hf loadings as low as 0.5 wt%, the extent of the EXAFS analysis at the W-L_{III} edge (10204 eV) had to be limited to the Hf-L_{II} edge (10739 eV, $k = 11.5$ Å^{-1}, Figure 3A) resulting in resolution loss of the radial distribution function (RDF) obtained by Fourier Transform (FT). This effect is clearly illustrated in Figure 3B, showing two RDF functions of the same sample (3WZ(ZrCl$_4$)923) calculated over different Δk intervals. In the first case, the FT is performed from 2.3 Å^{-1} up to the Hf-L_{II} edge (11.5 Å^{-1}) while in the second case, the FT is performed over a wider k range (up to 14.0 Å^{-1}).

Computing the FT over a wider k range mainly improves the peak resolution of the second and ensuing coordination shells, with the first shell remaining practically unaltered. Therefore it is not surprising that analysis of EXAFS spectra of tungstated zirconia catalysts is often mainly qualitative.[50, 55] Improvement of the peaks resolution beyond the first shell is of utmost importance to permit a reliable understanding of the local structure around tungsten atoms in the zirconia supported WO$_x$ phase. It has to be noted that another group[56] has recently tried to overcome the Hf problem at the W-L_{III}-edge by using W K-edge EXAFS at very high energy (69 524 eV) not commonly available on most EXAFS beamlines.

B.3b Reference tungsten compounds.

Tungsten reference compounds with well-known crystal structures were used on a comparative basis to provide insight on the structure of the WO$_x$ supported phase. Besides

sodium tungstate (Na_2WO_4, Fluka) and tungsten oxide (m-WO_3, Prolabo), two tungsten based isopolyanions, namely tetrabutylammonium hexatungstate ($[N(C_4H_9)_4]_2[W_6O_{19}]$, synthesized according to a published method[35]) and ammonium metatungstate (($NH_4)_6H_2W_{12}O_{40}$, Fluka) were studied by EXAFS.

Sodium tungstate. Sodium tungstate has a cubic structure[57] (*Fd3m, a* = 9.133(3) Å) where tungsten adopts a tetrahedral geometry with four oxygen atoms located at 1.819 Å. The FT of the corresponding EXAFS spectrum (not shown) was filtered in the 0.8-2.0 Å range so as to extract the experimental phase and amplitude parameters for the W-O shells; this reference was preferred because of the uniformity of the W-O bonds that have all the same length.

Tungsten oxide. Tungsten oxide (WO_3) exhibits a variety of crystalline structures. In the temperature range 290-593 K, the thermodynamically stable form is monoclinic. It consists of a network of *corner-shared* WO_6 distorted octahedra where the tungsten atoms are slightly displaced from the centre, giving rise to two non-equivalent types of octahedra, each one having six different W-O distances in the first coordination shell. The two types of WO_6 octahedra appear intercalated in the three-dimensional structure, resulting in a less ordered structure when compared to polytungstates. In the RDF, the first peak (0.8-2.0 Å) is assigned to the first oxygen shell,[58] the second peak (2.3-3.2 Å) to multiple-scattering effects within the first shell (W-O-O paths), and the third one (3.2-4.4 Å) to W second neighbours in corner-shared octahedra (Figure 4a, uncorrected for phase shift). The static disorder in m-WO_3 is somewhat high, resulting in larger Debye-Waller (DW) terms and peak broadening. This attribution was confirmed by simulation with the FEFF8 code[36] by comparing the results with and without introducing multiple-scattering effects based on the crystal structure[59] of m-WO_3.

Tetrabutylammonium hexatungstate. Hexatungstate $[N(C_4H_9)_4]_2[W_6O_{19}]$ crystallizes in the P-1 space group.[60] The polyanion $[W_6O_{19}]^{2-}$ exhibits a symmetric Lindqvist structure with six WO_6 octahedra sharing a common vertex localized on the central oxygen O_c. The octahedra

are distorted, with the tungsten atom being displaced towards terminal oxygens O_t. Besides the first oxygen shell, the second coordination sphere includes four tungsten atoms *sharing W-O_b-W edges* (whose average crystallographic distance is 3.289 Å) and farther a distant tungsten atom in "trans" position along the W-O_c-W axis (at 4.65 Å).[60] The experimental phase and amplitude for the W-W contribution were obtained by Fourier filtering in the 2.4-3.8 Å range. This reference was preferred to extract the W-W parameters because the four nearest W neighbours are found at similar distance (Figure 4b).

Ammonium metatungstate. The metatungstate anion $[W_{12}O_{40}H_2]^{6-}$ adopts a α-Keggin geometry with approximate overall T_d symmetry consisting of four groups of three edge shared WO_6 octahedra (W_3O_{13}).[61] These W_3O_{13} units are linked via oxygen bridges located on the octahedra corners. Therefore, each tungsten atom has two close tungsten neighbours *sharing edges* within the same W_3O_{13} unit, and two more distant tungsten atoms linked *through corners* from adjacent W_3O_{13} groups. Edge-shared octahedra present W-W distances about 0.4 Å shorter than corner-shared octahedra (3.30 and 3.71 Å respectively). Thus, the modulus of the FT for metatungstate shows two different W contributions in the second coordination sphere corresponding to these two distances (Figure 4c).

B.4 EXAFS study of WO$_x$/ZrO$_2$ catalysts

B.4a Qualitative analysis

In Figure 4d, the RDF plot of 19WZ(ZrCl$_4$)923 is compared to those of the three tungsten reference compounds described in B.3, which contain one type of tungsten neighbours (in octahedra sharing corners or edges) or both. In monoclinic WO_3, the peak at 3.7 Å is characteristic of W-W distances present in corner-sharing WO_6 units. Conversely, a peak at lower distance (3.2 Å) comes from the edge-sharing WO_6 units for the more condensed hexatungstate. As already mentioned, both types of W-W distances coexist in $[W_{12}O_{40}H_2]^{6-}$:

WO_6 units in each of the four W_3O_{13} groups share their edges, while interconnection between W_3O_{13} groups is done by means of corner-sharing.

Before trying to derive any structural parameters from the WO_x/ZrO_2 catalyst, a qualitative inspection of Figure 4 immediately shows that only W-W contributions ascribed to edge-shared units exists in 19WZ(ZrCl$_4$)923. It can be therefore stated that the W overlayer on zirconia is present as a polymeric structure in which tungstic units are interconnected through edges to form a more condensed structure than that of bulk oxide WO_3.

Moreover, an intense peak appears at 2.7 Å (uncorrected for phase-shift) which was not present on any of the reference RDF. Multiple scattering (MS) paths or ghost peaks might be at the origin of this lower distance peak. However, MS paths often lead to less intense and broader peaks than single scattering paths, as is shown on WO_3 RDF where MS peaks (2.3-3.2 Å) are barely discernable (Figure 4). Ghost peaks are known to arise whenever the backscattering amplitude is not a monotonic function of k, as it is the case for heavy elements and namely for tungsten.[15] But such ghost peaks appear only as weak shoulders in the W-W peak (at approximately 2.7 Å for hexa- and metatungstate) and not as an intense contribution. Hence, the high intensity of the peak observed at 2.7 Å in the catalyst 19WZ(ZrCl$_4$)923 may rather be explained by a W-Zr contribution, as will be shown below. While studying WO_3/TiO_2 catalysts, Hilbrig *et al.*[62] found a similar peak and attributed it to a W-Ti distance resulting from the anchorage of WO_x groups on the TiO_2 support. Wong *et al.*[55] observed this low distance peak on Al-promoted WO_x/ZrO_2 and proposed to assign it to a superposition of W-W and W-Zr shells.

No substantial differences were found for the two catalysts containing quite different tungsten loadings and calcined at the same temperature (3WZ(ZrCl$_4$)923 and 19WZ(ZrCl$_4$)923, Figure 5). This finding supports the fact that polyoxo corner-shared WO_x domains are present even at low tungsten contents, when dispersion is high (2.0 W nm^{-2}), in agreement with Raman data

(observation of the antisymmetric stretching mode of bridging oxygens W-O$_b$-W at 830 cm^{-1}; see electronic supplementary information) and with literature results.[63]

Some modifications of the RDF are observed for 19WZ(ZrCl$_4$)1098 (Figure 5c): the intensity of the W-W corner-shared peak diminishes while a new broad peak at 3.7 Å emerges. However, in this sample, XRD and Raman (major bands at 806, 710 and 271 cm^{-1}, see electronic supplementary information) revealed the formation of WO$_3$ crystallites which explains the fact that the EXAFS signal corresponds to a mixture of bulk WO$_3$ (peak at ca. 3.7 Å) and dispersed polyoxostructures.

B.4b Quantitative analysis

A more detailed insight on the local structure around W atoms was obtained by simulating the EXAFS spectra. The RDFs presented in Figure 5 were back-Fourier transformed in the 0.7-5.0 Å range (ΔR) so as to filter off the high frequency noise. Thanks to the good quality of the EXAFS spectra obtained over Hf-free zirconia, the number of independent points was high enough to accommodate all the model parameters and still leave more than 10 degrees of freedom (according to the Nyquist theorem $N_{idp} = \dfrac{2\Delta k \Delta R}{\pi} + 2$).[15]

Catalyst 3WZ(ZrCl$_4$)923. The fit of the EXAFS spectrum of the low tungsten loading sample (3WZ(ZrCl$_4$)923) was carried out by considering five distinct shells (Table 3 and Figure 6A). The first two shells are undoubtedly ascribed to oxygen atoms in the first coordination sphere that account for the two peaks of the RDF between 1 and 2.5 Å: 2.92 oxygens located at 1.79 Å and 0.42 oxygen located at 2.50 Å. This latter distance should be taken cautiously, since even in highly distorted structures like WO$_3$·H$_2$O the farthest oxygen is found at 2.34 Å.[58]

As can be seen in Figure 5, a peak seen at 2 Å (uncorrected for phase shift) is indeed present for the three catalysts and may be ascribed to a long W-O bond (equivalent to the W-O$_c$ distance in hexatungstate). This peak, however, becomes practically absent for

19WZ(ZrCl$_4$)923 and 19WZ(ZrCl$_4$)1098 after filtering and modelling (Figures 6B and 6C), because the use of experimental phases and amplitudes restricts the EXAFS analysis to the 3.5 < k < 14 Å^{-1} range, thereby decreasing the resolution of the corresponding RDF.

The peak seen at 2.8 Å (uncorrected for phase shift) was correctly fitted by considering a Zr neighbour at 3.14 Å with an average coordination number of 0.76. The observation of Zr atoms from the support indicates that the WO$_x$ phase is well dispersed onto the zirconia surface. An additional contribution ascribed to 4 W atoms in the second coordination sphere arises at 3.27 Å which is a distance characteristic of edge-sharing structures. This confirms that even at low tungsten surface densities (2.1 W nm^{-2}), polymeric WO$_x$ edge-sharing structures already exist. Finally, another peak probably arising from the zirconia support emerges at 4.23 Å, reinforcing the idea of well-dispersed WO$_x$ structures interacting with the zirconia surface.

Catalyst 19WZ(ZrCl$_4$)923. Increasing the tungsten content from 3 to 19 wt% WO$_3$ while keeping the calcination temperature at 923 K does not seem to influence the RDF, as shown in Figure 6B, although the tungsten surface density has increased to 11.4 W nm^{-2}. In fact the simulation results (Table 3) indicate that the same backscatterers are present at exactly the same interatomic distances (within the experimental error), except for the longest W-O$_c$ distance which is no longer visible and was discarded in the fitting procedure. The only major change lies in the intensity of the peak of the W-O first shell, since the coordination number increases to 3.79 instead of 2.92 for 3WZ(ZrCl$_4$)923. The coordination number of the W-Zr distance in the second coordination shell increases also slightly to 1, within the error margin, but the coordination number due to the W second neighbours is roughly the same as in sample 3WZ(ZrCl$_4$)923 (4.13). Hence, EXAFS data suggest that no WO$_x$ domain growth occurs when the tungsten surface density increases from 2.0 to 11.4 W nm^{-2}.

Catalyst 19WZ(ZrCl₄)1098. As the calcination temperature increases from 923 to 1098 K for the WO_x/ZrO_2 sample containing 19% wt. WO_3, the specific surface area decreases and the surface density of WO_x reaches 12.3 W nm^{-2}. Microcrystalline WO_3 is formed under these conditions, as mentioned previously. Therefore it is not surprising that an additional peak arises in the RDF (Table 3, Figure 6C). It is ascribed to an incipient W-W contribution ($CN = 0.29$) at 3.80 Å, similar to the one found on pure m-WO_3.[59] Besides this new W-W contribution, no substantial changes can be noticed regarding the position of the remaining peaks. The fitted parameters yielded the same interatomic distances as found over the other samples. However the coordination number of the first W neighbours increases up to 5.06, which evidences an important growth of the WO_x domains.

B.5 Structural model.

B.5a State of the art

Barton *et al*.[50] were the first to report XAS data on the WO_x/ZrO_2 catalytic system. Their W-L_I XANES data showed that tungsten adopts a distorted octahedral symmetry over a wide range of WO_x concentrations, while the W surface density is known to strongly influence the catalytic activity. Therefore these different catalytic behaviours could not be assigned to changes in the coordination environment around W atoms. Moreover, analysis of the RDFs obtained at the W-L_{III} edge led the authors to conclude that W atoms in WO_x/ZrO_2 reside in distorted octahedral structures similar to bulk WO_3, despite a W-W peak that actually appears at a slightly lower distance compared to WO_3. A more detailed quantitative analysis of their EXAFS spectra was made difficult due to the presence of an Hf impurity.

Valigi *et al*.[64] analyzed EXAFS data beyond the first shell in WO_x/ZrO_2 catalysts leached with ammonia so as to remove weakly surface bound WO_x species. They found evidence for both W-Zr and W-W contributions in the second coordination sphere of W at 2.87 Å and 3.03 Å

respectively. An additional multiple scattering W-O-O contribution at 3.74 Å was added to better fit the data. These values were systematically lower by 0.27 Å than the W-Zr and W-W distances found in our work. Furthermore our W-W shortest distance is known to be present in some molecular references as shown above, but the distance reported by Valigi et al.[64] is not known in any well defined molecular tungstate.

Wong et al.[55] studied Al-doped WO_x/ZrO_2 catalysts. Although the presence of an Hf impurity was also limiting the EXAFS data range, their RDF on Al-free samples are much better defined than those obtained by Barton et al.[50], and closely resemble our own data. Namely, two sharp peaks arise in the second coordination sphere of W, attributed to W-Zr and W-W scatterers. The authors underline the fact that the W-W peak appears at 0.31-0.37 Å lower than for bulk WO_3, in agreement with our observations. Unfortunately no quantitative analysis was carried out to further elucidate the WO_x local structure.

Yamamoto et al. [56] used W-K edge EXAFS (in order to avoid any interference from the Hf L_2 edge) and W-L_I edge to study WO_x/ZrO_2 catalysts. These authors pointed out that the tungsten surface phase was clearly different from a bulk WO_3 phase.

On a related system (WO_x/TiO_2), Yamazoe et al. [65] showed recently that a detailed compared analysis of the W L_{III} and L_I edges may lead to a fine description of the W symmetry. In this case it was surprisingly shown that the coordination of W was changing from six-fold to four-fold when increasing the W content.

B.5b Proposed model

The data presented above along with the simulated EXAFS spectra allow us to propose a structural model able to describe the local environment surrounding W atoms in the WO_x phase of tungstated zirconia samples.

The first coordination sphere around W is made of oxygen atoms that may exhibit a wide range of interatomic distances, depending on the local symmetry of the WO_6 units. However, coordination numbers were always below 6 for the three catalysts studied, contrarily to what should be expected from octahedral coordination. As mentioned by Prins and Köningsberger,[13] intensity decrease in the first coordination sphere tends to occur in disordered systems, like MoO_3/Al_2O_3, due to severe distortion. The destructive interference introduced by multiple close distances is at the origin of reduced coordination numbers, although the Debye-Waller term should provide a correction for this effect. However, Debye-Waller disorder assumes a Gaussian distribution of distances, which may not be a reasonable approximation in highly disordered systems and especially in tungstates chemistry. The first coordination sphere could be well described by considering approximately three W-O neighbours at 1.80 Å on the three catalysts and the remaining neighbours at longer distances. Nevertheless, the greatest interest resides in the second coordination sphere around W, where both W-Zr and W-W contributions are detected. One W-Zr peak is found at 3.14 Å on the RDFs of all three catalysts. The uniformity of the W(-O-)Zr distance and coordination number holds for the three catalysts studied, regardless of the tungsten surface density. This similarity provides convincing evidence that WO_x clusters are perfectly dispersed onto the zirconia surface to form a bidimensional overlayer that is directly anchored to the ZrO_2 surface by means of W-O-Zr bonds. It has to be noted that these surface bonds are shorter than those observed in Zirconium-substituted molecular isopolytungstates.[66,67]

Isolated tungsten species are not the major species in any of the samples studied, even at low tungsten surface density (2.1 W nm^{-2}). Instead, the appearance of W nearest neighbours at about 3.3 Å (indicative of edge-shared octahedra) and the absence of W neighbours at 3.7 Å (corner-shared octahedra) supports the fact that bidimensional slabs are formed by interconnected edge-sharing WO_6 octahedra, as represented in Figure 7A. Such slabs could

give a realistic description of the "Zr-Stabilized WO_3 nanoparticles" recently proposed by Ross-Medgaarden et al.[52]

The proposed surface structure is deduced from EXAFS data obtained in air, but it is highly probable that the W speciation would remain unaffected in dehydrated conditions. As a matter of fact, Yamamoto et al.[56] showed recently with XANES at the W L_1-edge for WO_x/ZrO_2 catalysts that for high W loadings (where polytungstates are expected) the W symmetry was unaffected by hydration/dehydration treatments.

This type of finite slab gives rise to four different tungsten environments, depending on where the central tungsten atom is located. Inside the slab, tungsten may have as high as six nearest W atoms placed at the same distance **d** while tungsten atoms located on the slab corners will have 2 or 3 neighbours, depending on which corner is considered, and those located on the slab edges will have 4 neighbours. As a consequence, the average coordination number around tungsten atoms in bidimensional slabs of finite size is always less than 6. Considering the slab geometry of Figure 7A and considering the same number of WO_6 units on both sides, the theoretical average coordination number is given by Eq. 2 as a function of the number of lateral WO_6.

Eq. 2
$$CN = \frac{10 + 16 \cdot (n-2) + 6 \cdot (n-2)^2}{4 + 4 \cdot (n-2) + (n-2)^2}$$

A graphical representation of this expression is provided in Figure 7B.

When the slabs are small enough (less than 6 lateral units) it is possible to estimate their size with enough accuracy on the basis of the average coordination number as determined from EXAFS, for example. The fitted coordination numbers for the three WO_x/ZrO_2 catalysts studied are represented in Figure 7B as horizontal lines, intersecting the theoretical curve.

Within the experimental error, it can be concluded that for both 3WZ(ZrCl$_4$)923 and 19WZ(ZrCl$_4$)923 catalysts, WO$_x$ could exist in the form of polymeric bidimensional clusters having 4 WO$_6$ units on each side.

One would expect the size of the WO$_x$ slabs to increase as the tungsten content increases while keeping constant the calcination temperature. However there is an important effect that must also be taken into account. Increasing the tungsten content also stabilizes a larger fraction of tetragonal zirconia. Hence, for 19WZ(ZrCl$_4$)923, WO$_x$ species spread over a zirconia surface that is 100% v/v t-ZrO$_2$, while for 3WZ(ZrCl$_4$)923 there is only 61% v/v t-ZrO$_2$.[68] Yet, for both samples the size of the WO$_x$ bidimensional slabs does not change. This suggests the preferential anchorage of WO$_x$ domains on the surface of tetragonal zirconia relative to monoclinic zirconia. Hence, care must be taken when referring to tungsten surface densities where both monoclinic and tetragonal phases are present.

Increasing the calcination temperature of the 19 wt% WO$_3$ sample up to 1098 K results in the growth of polytungstate domains, with the corresponding coordination number reaching around five W nearest neighbours. In this range it becomes difficult to accurately predict the exact size of the WO$_x$ slabs from Eq. 2, although the saturation loading is reached since tridimensional microcrystalline WO$_3$ starts to segregate.

CONCLUSION

Two case studies have been selected in order to highlight the ability of EXAFS spectroscopy to provide a comprehensive description of the molecular structure of mononuclear metal-complexes (Ni bisglycinate) or supported nanophases (tungsten oxide) dispersed on an oxide support (alumina and zirconia respectively). A particular emphasis has been put on the characterization of metal-support interaction, *i.e.*, the formation of metal-oxygen-support bonds.

The first example concerns the grafting of neutral Ni bisglycinate complexes onto alumina. It is shown that the structure of the complex is preserved upon its adsorption while Ni-O(H)-Al bonds are formed right from the impregnation step providing that the impregnation solution is moderately heated. Conversely, for room temperature impregnation, nickel bisglycinate probably interacts with the support by hydrogen bonding.

The second example deals with tungstated zirconia (WO_x/ZrO_2) which are promising heterogeneous catalysts for the isomerization of light alkanes. Based on EXAFS spectroscopy, it is possible to establish a geometric model that explains both interatomic distances and mean coordination numbers associated with W centres. It is unambiguously shown that W exists in the form of bidimensional polytungstate nanodomains (WO_x) with WO_6 units linked by sharing edges only even at low surface densities (2.0 $W.nm^{-2}$). Such 2D slabs have never been reported before in the literature since it is usually assumed that W domains are made up of a polytungstate-like overlayer (*i.e.*, three-dimensional network of edge-shared and corner-shared WO_6 groups), It may be inferred that the uniqueness of the WO_x/ZrO_2 couple in acid catalysis is related to the ability of zirconia to stabilize this 2D surface structure. Future work will be needed to gain more insight into the reducibility of the proposed edge-shared W structure and its correlation with the generation of strong acidity. The observation of a W-Zr contribution accounts for the excellent dispersion of tungstic species on the zirconia surface,

because the nanodomains are grafted onto the support through W-O-Zr bonds after high temperature calcination.

More progress in the molecular-scale understanding of heterogeneous catalytic systems can be expected with EXAFS spectroscopy by combining this technique with other complementary characterization methods as shown by the growing interest on this topic. [69, 70]. Combining spectroscopic measurements on the same sample at the same time should bring several benefits: avoiding problems related to sample ageing and synthesis reproducibility for separate experiments, improving the time/temperature correlation of surface transformation probed by different techniques, checking for possible X-ray beam damage during EXAFS data collection and maybe even more importantly constraining and thus improving EXAFS data analysis. Combination of Raman and EXAFS for investigating alumina-supported Mo oxide catalysts for example[69] showed that Raman is a key method for gaining insight in Mo speciation while EXAFS spectroscopy is able to give a quantitative information with constraints provided by Raman.

Further development will also come from the combination of techniques coupled with time-resolved XAS spectroscopy allowing dynamic characterization of heterogeneous catalysts throughout different preparation steps and during catalytic experiments (Operando spectroscopy) in real time. A few recent publications have already shown the potential of combined SAXS/WAXS/Quick-EXAFS[71], UV-Vis/Raman/Energy-dispersive EXAFS[72] or UV-vis/Energy-dispersive EXAFS[73] measurements for achieving temporal resolution in the sub-second time frame for characterizing materials of catalytic interest.

ACKNOWLEDGMENTS

ELECTRONIC SUPPLEMENTARY INFORMATION

UV-Vis, FTIR and Raman spectroscopy characterizations mentioned in the text are available as Electronic Supplementary Information.

Figure 1. FT (k = 2.2-11.8 Å^{-1}) of k^3 weighted EXAFS spectra of: a) nickel bisglycinate in aqueous solution (0.08 mol.L^{-1}), b) crystals of nickel bisglycinate, c) NGamb prepared at ambient temperature, d) NG333 prepared at 333 K.

Figure 2. Absolute and imaginary part of the k^3 weighted FT EXAFS spectra of: a) nickel bisglycinate in aqueous solution, b) NGamb prepared at room temperature, c) NG333 prepared at 333 K. Experimental (full lines) and simulated (dashed lines) spectra are shown. The experimental spectra were back-Fourier filtered in the 0.7-3.1 Å range.

Figure 3.   A) Normalized X-ray absorption coefficient $\boldsymbol{\mu}(E)$ for two dried (383 K) catalyst samples containing similar tungsten contents (19 wt. % WO_3). Catalysts were prepared using zirconium hydroxide freshly precipitated from a) Hf-containing $ZrOCl_2 \cdot 8H_2O$ (Fluka) and b) from Hf-free $ZrCl_4$ (Aldrich);

        B) Radial distribution functions obtained from k^3-weighted FT of W-L_{III} EXAFS signals of 3WZ(ZrCl$_4$)923 over a) Δk = 2.3-11.5 Å^{-1} and b) Δk = 2.3-14.0 Å^{-1}.

Figure 4. FT (k = 2.3-14.0 Å^{-1}) of k^3 weighted EXAFS spectra of tungsten references: a) monoclinic tungsten oxide, b) tetrabutylammonium hexatungstate and c) ammonium metatungstate as well as d) a tungstated zirconia catalyst (19WZ(ZrCl$_4$)923). The corresponding FT have not been phase or amplitude corrected.

Figure 5. FT (k = 2.3-14.0 Å^{-1}) of k^3-weighted EXAFS spectra of WO$_x$/ZrO$_2$ catalysts: a) 3WZ(ZrCl$_4$)923, b) 19WZ(ZrCl$_4$)923 and c) 19WZ(ZrCl$_4$)1098.

Figure 6. Absolute and imaginary parts of the k^3-weighted FT EXAFS spectra of samples A) 3WZ(ZrCl$_4$)923, B) 19WZ(ZrCl$_4$)923 and C) 19WZ(ZrCl$_4$)1098. Experimental (full lines) and simulated (dashed lines) spectra are shown. The experimental spectra were back-Fourier filtered in the 0.7-5.0 Å range.

Figure 7. A) Bidimensional slab consisting of edge-sharing WO$_6$ units. If the W-W edge-shared interatomic distance, d, is assumed to be equal then $\alpha = 120°$; B) Average coordination number (CN) around W for bidimensional edge-sharing structures with different sizes. The actual coordination number (CN) derived from EXAFS for samples 3WZ(ZrCl$_4$)923 (dashed line), 19WZ(ZrCl$_4$)923 (full line) and 19WZ(ZrCl$_4$)1098 (dotted line) are also shown.

REFERENCES

1   E. Marceau, X. Carrier, M. Che, O. Clause and C. Marcilly, in *Handbook of Heterogeneous Catalysis*, ed. G. Ertl, H. Knözinger, F. Schüth and J. Weitkamp, Wiley-VCH, Weinheim, 2008, pp. 467-484.
2   B. M. Weckhuysen, in *In-situ Spectroscopy of Catalysts*, ed. B. M. Weckhuysen, ASP, Stevenson Ranch, 2005, pp. 1-11.
3   X. Carrier, E. Marceau and M. Che, *Pure Appl. Chem.*, 2006, **78**, 1039-1055.
4   E. Marceau, in *Nanocatalysis*, ed. D. Y. Murzin, Research Signpost, Kerala (India), 2006, pp. 127-175.
5   J. A. Bergwerff and B. M. Weckhuysen, in *Handbook of Heterogeneous Catalysis*, ed. G. Ertl, H. Knözinger, F. Schüth and J. Weitkamp, Wiley-VCH, Weinheim, 2008, vol. 2, pp. 1188-1197.
6   G. Busca, *J. Raman Spectrosc.*, 2002, **33**, 348-358.
7   I. E. Wachs, *Catal. Today*, 1996, **27**, 437-455.
8   I. E. Wachs, in *Metal Oxides: Chemistry and Applications*, ed. J. L. G. Fierro, CRC Press, Boca Raton, 2006, pp. 2-30.
9   R. Radhakrishnan, C. Reed, S. T. Oyama, M. Seman, J. N. Kondo, K. Domen, Y. Ohminami and K. Asakura, *J. Phys. Chem. B*, 2001, **105**, 8519-8530.
10   S. Chempath, Y. Zhang and A. T. Bell, *J. Phys. Chem. C*, 2007, **111**, 1291-1298.
11   E. L. Lee and I. E. Wachs, *J. Phys. Chem. C*, 2007, **111**, 14410-14425.
12   D. C. Koningsberger and D. E. Ramaker, in *Handbook of Heterogeneous Catalysis*, ed. G. Ertl, H. Knözinger, F. Schüth and J. Weitkamp, Wiley-VCH, Weinheim, 2008, vol. 2, pp. 774-803.
13   R. Prins and D. C. Koningsberger, in *X-Ray Absorption. Principles, Applications, Techniques of EXAFS, SEXAFS and XANES*, ed. D. C. Koningsberger and R. Prins, John Wiley & Sons, New York, 1988, vol. 92, pp. 321-372.
14   J. A. van Bokhoven, T. Ressler, F. M. F. de Groot and G. Knopp-Gericke, in *In-situ Spectroscopy of Catalysts*, ed. B. M. Weckhuysen, ASP, Stevenson Ranch, 2004, pp. 123-144.
15   D. C. Koningsberger, B. L. Mojet, G. E. van Dorsen and D. E. Ramaker, *Top. Catal.*, 2000, **10**, 143-155.
16   S. Boujday, J.-F. Lambert and M. Che, *Chem. Phys. Chem.*, 2004, **5**, 1003-1013.
17   L. Medici and R. Prins, *J. Catal.*, 1996, **163**, 28-37.
18   S. N. Towle, J. R. Bargar, G. E. Brown,Jr. and G. A. Parks, *J. Coll. Interf. Sci.*, 1999, **217**, 312-321.
19   F. Rataboul, C. Copéret, L. Lefort, A. de Mallmann, J. Thivolle-Cazat and J. M. Basset, *Dalton Trans.*, 2007, 923-927.
20   M. Jezequel, V. Dufaud, M. J. Ruiz-Garcia, F. Carrillo-Hermosilla, U. Neugebauer, G. P. Niccolai, F. Lefebvre, F. Bayard, J. Corker, S. Fiddy, J. Evans, J. P. Broyer, J. Malinge and J. M. Basset, *J. Am. Chem. Soc.*, 2001, **123**, 3520-3540.
21   B. Rhers, A. Salameh, A. Baudouin, E. A. Quadrelli, M. Taoufik, C. Copéret, F. Lefebvre, J. M. Basset, X. Solans-Monfort, O. Eisenstein, W. L. Lukens, L. P. H. Lopez, A. Sinha and R. R. Schrock, *Organometallics*, 2006, **25**, 3554-3557.
22   A. W. Moses, N. A. Ramsahye, C. Raab, H. D. Leifeste, S. Chattopadhyay, B. F. Chmelka, J. Eckert and S. L. Scott, *Organometallics*, 2006, **25**, 2157-2165.

23   D. E. Keller, S. M. K. Airaksinen, A. O. Krause, B. M. Weckhuysen and D. C. Koningsberger, *J. Am. Chem. Soc.*, 2007, 3189-3197.

24   Y. Hao and B. C. Gates, *J. Catal.*, 2009, **263**, 83-91.

25   P. Burattin, M. Che and C. Louis, *J. Phys. Chem. B*, 1997, **101**, 7060-7074.

26   J. Y. Carriat, M. Che, M. Kermarec, M. Verdaguer and A. Michalowicz, *J. Am. Chem. Soc.*, 1998, **120**, 2059-2070.

27   a) O. Clause, M. Kermarec, L. Bonneviot, F. Villain and M. Che, *J. Am. Chem. Soc.*, 1992, **114**, 4709-4717; b) O. Clause, L. Bonneviot, M. Che, H. Dexpert, *J. Catal.*, 1991, **130**, 21-28.

28   J. B. d'Espinose de la Caillerie, M. Kermarec and O. Clause, *J. Am. Chem. Soc.*, 1995, **117**, 11471-11481.

29   S. N. Towle, J. R. Bargar, G. E. Brown, Jr. and G. A. Parks, *J. Coll. Interf. Sci.*, 1997, **187**, 62-82.

30   A. Manceau, M. Schlegel, K. L. Nagy and L. Charlet, *J. Coll. Interface Sci.*, 1999, **220**, 181-197.

31   A. C. Scheinost and D. L. Sparks, *J. Coll. Interface Sci.*, 2000, **223**, 167-178.

32   M. Mhamdi, E. Marceau, S. Khaddar-Zine, A. Ghorbel, M. Che, Y. B. Taarit and F. Villain, *Catal. Lett.*, 2004, **98**, 135-140.

33   M. Mhamdi, E. Marceau, S. Khaddar-Zine, A. Ghorbel, M. Che, Y. B. Taarit and F. Villain, *Z. Phys. Chem.*, 2005, **219**, 963-978.

34   A. Michalowicz, *Logiciels pour la Chimie*, Société Francaise de Chimie, Paris, 1991.

35   M. Fournier, in *Inorganic Syntheses*, ed. P. G. Alvin, John Wiley, New York, 1990, vol. 27, pp. 80-81.

36   A. L. Ankudinov, B. Ravel, J. J. Rehr and S. D. Conradson, *Phys. Rev. B*, 1998, **58**, 7565-7576.

37   F. Averseng, M. Vennat and M. Che, in *Handbook of Heterogeneous Catalysis*, ed. G. Ertl, H. Knözinger, F. Schüth and J. Weitkamp, Wiley-VCH, Weinheim, 2008, vol. 1, pp. 522-539.

38   F. Négrier, E. Marceau, M. Che, J.-M. Giraudon, L. Gengembre and A. Löfberg, *J. Phys. Chem. B*, 2005, **109**, 2836-2845.

39   K.-Q. Sun, E. Marceau and M. Che, *Phys. Chem. Chem. Phys.*, 2006, **8**, 1731-1738.

40   V. Rodriguez-Gonzalez, E. Marceau, M. Che and C. Pepe, *J.Solid State Chem.*, 2007, **180**, 3469-3478.

41   V. Rodriguez-Gonzalez, E. Marceau, P. Beaunier, M. Che and C. Train, *J.Solid State Chem.*, 2007, **180**, 22-30.

42   G. Busca, *Chem. Rev.*, 2007.

43   M. Hino and K. Arata, *J. Chem. Soc., Chem. Commun.*, 1988, 1259-1260.

44   M. Scheithauer, T. K. Cheung, R. E. Jentoft, R. K. Grasselli, B. C. Gates and H. Knözinger, *J. Catal.*, 1998, **180**, 1-13.

45   S. Kuba, P. Concepción Heydorn, R. K. Grasselli, B. C. Gates, M. Che and H. Knözinger, *Phys. Chem. Chem. Phys.*, 2001, **3**, 146-154.

46   C. D. Baertsch, K. T. Komala, Y.-H. Chua and E. Iglesia, *J. Catal.*, 2002, **205**, 44-57.

47   D. G. Barton, S. L. Soled and E. Iglesia, *Top. Catal.*, 1998, **6**, 87-99.

48   J. Macht, C. D. Baertsch, M. May-Lozano, S. L. Soled, Y. Wang and E. Iglesia, *J. Catal.*, 2004, **227**, 479-491.

49   S. Kuba, P. Lukinskas, R. K. Grasselli, B. C. Gates and H. Knözinger, *J. Catal.*, 2003, **216**, 353-361.

50   D. G. Barton, S. L. Soled, G. D. Meitzner, G. A. Fuentes and E. Iglesia, *J. Catal.*, 1999, **181**, 57-72.

51   S. De Rossi, G. Ferraris, M. Valigi and D. Gazzoli, *Appl. Catal. A*, 2002, **231**, 173-184.

52   E. I. Ross-Medgaarden, W. V. Knowles, T. Kim, M. S. Wong, W. Zhou, C. J. Kiely and I. E. Wachs, *J. Catal.*, 2008, **256**, 108–125.

53   H. Toraya, M. Yoshimura and S. Somiya, *J. Am. Ceram. Soc.*, 1984, **67**, C119-C121.

54   M. Valigi, D. Gazzoli, I. Pettiti, G. Mattei, S. Colonna, S. De Rossi and G. Ferraris, *Applied Catalysis, A: General*, 2002, **231**, 159-172.

55   S.-T. Wong, T. Li, S. Cheng, J.-F. Lee and C.-Y. Mou, *J. Catal.*, 2003, **215**, 45-56.

56   T. Yamamoto, A. Orita and T. Tanaka, *X-Ray Spectrom.*, 2008, **37**, 226-231.

57   K. Okada, H. Morikawa, F. Marumo and S. Iwai, *Acta Cryst.*, 1974, **B30**, 1872.

58   J. Purans, A. Kuzmin and C. Guery, *Proceedings of SPIE-The International Society for Optical Engineering*, 1997, **2968**, 174-179.

59   B. O. Loopstra and H. M. Rietveld, *Acta Cryst., Section B*, 1969, **25**, 1420-1421.

60   J. Fuchs, W. Freiwald and H. Hartl, *Acta Cryst. B*, 1978, **B34**, 1764-1770.

61   M. T. Pope, *Heteropoly and Isopoly Oxometalates*, Springer-Verlag, Berlin, 1983.

62   F. Hilbrig, H. E. Göbel, H. Knözinger, H. Schmelz and B. Lengeler, *J. Phys. Chem.*, 1991, **95**, 6973-6978.

63   M. Scheithauer, R. K. Grasselli and H. Knoezinger, *Langmuir*, 1998, **14**, 3019-3029.

64   M. Valigli, D. Gazzoli, I. Pettiti, G. Mattei, S. Colonna, S. D. Rossi and G. Ferraris, *Appl. Catal. A*, 2002, **231**, 159-172.

65   S. Yamazoe, Y. Hitomi, T. Shishido and T. Tanaka, *J. Phys. Chem. C*, 2008, **112**, 6869-6879.

66   H. Carabineiro, R. Villanneau, X. Carrier, P. Herson, F. Lemos, F. Ramoa Ribeiro, A. Proust and M. Che, *Inorg. Chem.*, 2006, **45**, 1915-1923.

67   R. Villanneau, H. Carabineiro, X. Carrier, R. Thouvenot, P. Herson, F. Lemos, F. Ramoa Ribeiro and M. Che, *J. Phys. Chem. B*, 2004, **108**, 12465-12471.

68   H. Carabineiro, Universidade Técnica de Lisboa/Université P. & M. Curie, 2005.

69   V. Briois, S. Belin, F. Villain, F. Bouamrane, H. Lucas, R. Lescouezec, M. Julve, M. Verdaguer, M. S. Tokumoto, C. V. Santilli, S. H. Pulcinelli, X. Carrier, J. M. Krafft, C. Jubin and M. Che, *Phys. Scr.*, 2005, **T115**, 38-44.

70   S. J. Tinnemans, J. G. Mesu, K. Kervinen, T. Visser, T. A. Nijhuis, A. M. Beale, D. E. Keller, A. M. J. van der Eerden and B. M. Weckhuysen, *Catal. Today*, 2006, **113**, 3-15.

71   A. M. Beale, A. M. J. van der Eerden, S. D. M. Jacques, O. Leynaud, M. G. O'Brien, F. Meneau, S. Nikitenko, W. Bras and B. M. Weckhuysen, *J. Am. Chem. Soc.*, 2006, **128**, 12386-12387.

72   A. M. Beale, A. M. J. van der Eerden, K. Kervinen, M. A. Newtonb and B. M. Weckhuysen, *Chem. Commun.*, 2005, 3015–3017.

73   G. Guilera, M. A. Newton, C. Polli, S. Pascarelli, M. Guino and K. K. Hii, *Chem. Commun.*, 2006, 4306-4308.

Table 1. Summary of the EXAFS fitting results for the nickel bisglycinate systems.[a]

Sample	Pair	CN	R (Å)	$\Delta\sigma$ ($\mathring{A}^{-1}$)	ΔE_0 (eV)	R^2 (%)
Nickel bisglycinate	Ni-O	4.00	2.09	0	0.9	
0.08 mol.L^{-1} solution	Ni-N	2.00	2.09	0	0.2	0.2
	Ni-C	4.00	2.88	0.055	-0.6	
NGamb	Ni-O	4.00	2.09	0.015	0.9	
	Ni-N	2.00	2.09	0.015	0.2	0.5
	Ni-C	4.00	2.88	0.065	-0.6	
NG333	Ni-O	4.00	2.09	0.015	0.9	
	Ni-N	2.00	2.10	0.015	0.2	1.5
	Ni-C	4.00	2.86	0.078	1.0	
	Ni-Al	1.83	3.05	0.105	4.2	

[a] Standard errors in EXAFS are ± 0.02 Å for distances and ± 10 % for coordination numbers.

Table 2. Sample denominations with the corresponding surface area, W content, W surface density and tetragonal volumetric fraction.

Sample denomination	S_{BET} $(m^2.g^{-1})$	% WO_3	W surface density (atom.nm^{-2})	% Vol. Fraction of t-ZrO_2 [a]
3WZ(ZrCl$_4$)923	37	2.9	2.0	61
19WZ(ZrCl$_4$)923	45	19.7	11.4	100
19WZ(ZrCl$_4$)1098	39	18.5	12.3	96

[a] Tetragonal *vs*. monoclinic volumetric fraction determined from the integrated intensities of the tetragonal and monoclinic reflection in the XRD pattern.[53]

**Table 3.** Summary of the EXAFS fitting results for the hafnium free WO_x/ZrO_2 catalysts.[a]

| Sample	Pair	CN	R (Å)	$\Delta\sigma$ (Å^{-1})	ΔE_0 (eV)	R^2 (%)
3WZ(ZrCl$_4$)923	W-O	2.92	1.79	0.063	-12.6	
	W-O	0.42	2.50	0.002	-12.6	
	W-Zr	0.76	3.14	0.078	-1.4	2.1
	W-W	3.95	3.27	0.108	0.8	
	W-Zr	1.68	4.23	0.100	-1.4	
19WZ(ZrCl$_4$)923	W-O	3.79	1.80	0.078	-10.3	
	W-Zr	0.91	3.13	0.087	-0.3	
	W-W	4.13	3.30	0.111	3.6	2.1
	W-Zr	2.00	4.23	0.104	-0.3	
19WZ(ZrCl$_4$)1098	W-O	2.73	1.79	0.053	-12.0	
	W-Zr	0.94	3.14	0.087	0.4	
	W-W	5.06	3.25	0.135		3.3
	W-W	0.29	3.80	0.052	-0.7	
	W-Zr	1.91	4.27	0.103	0.4	

[a] Standard errors in EXAFS are ± 0.02 Å for distances and ± 10 % for coordination numbers.
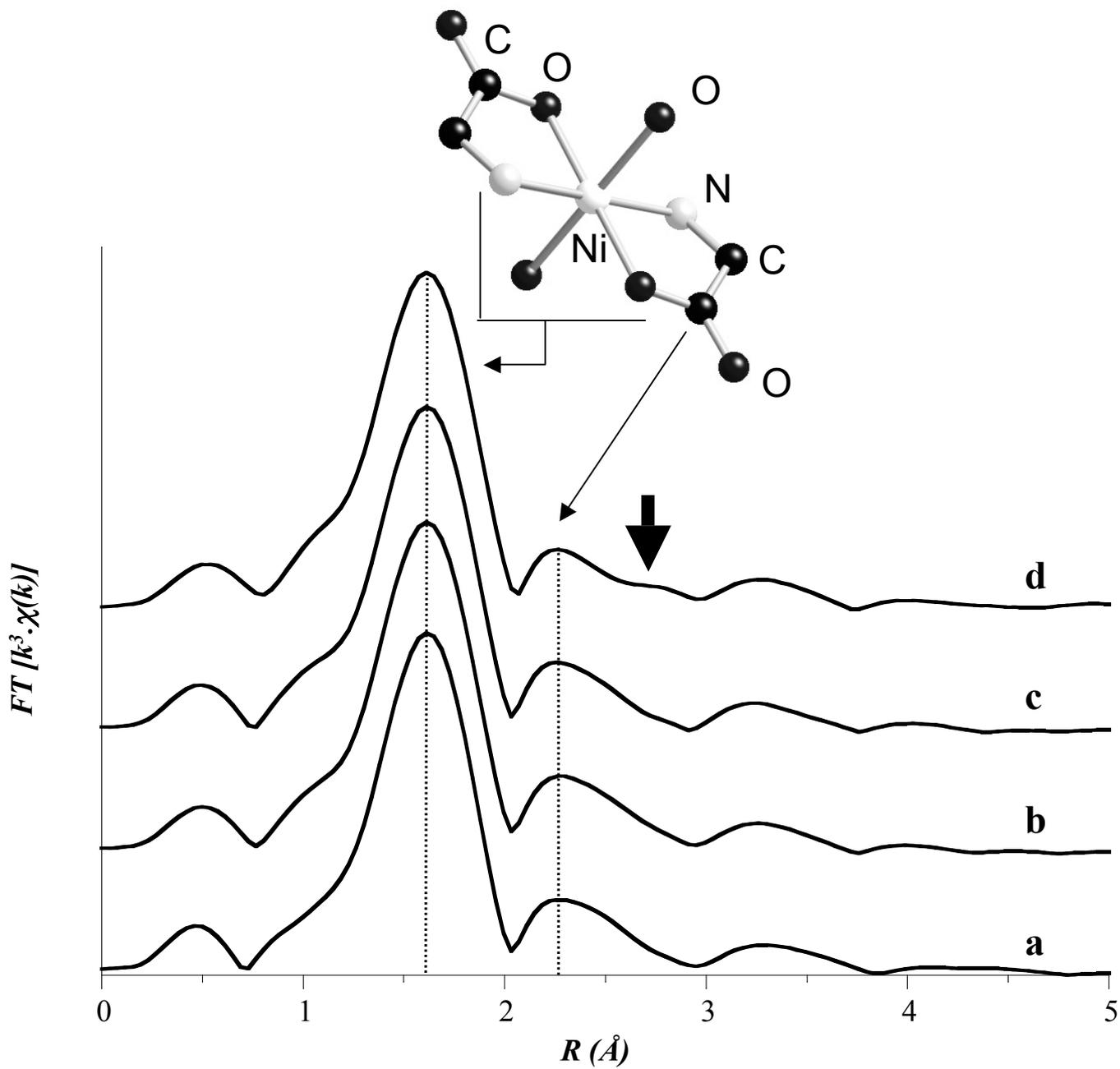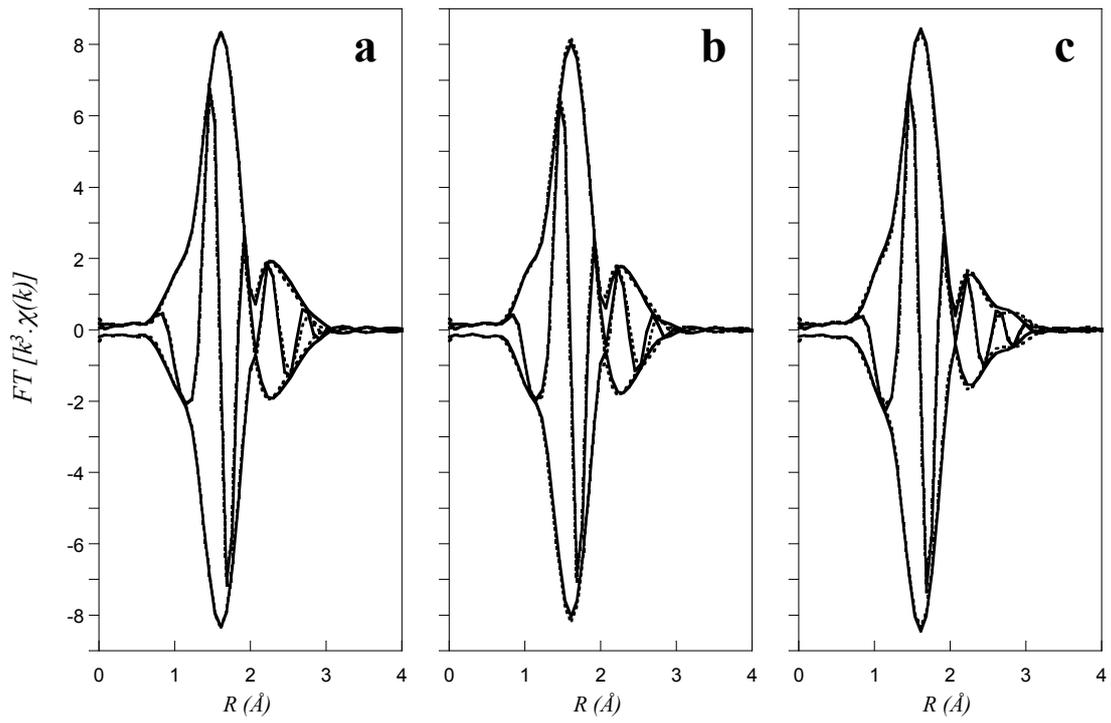
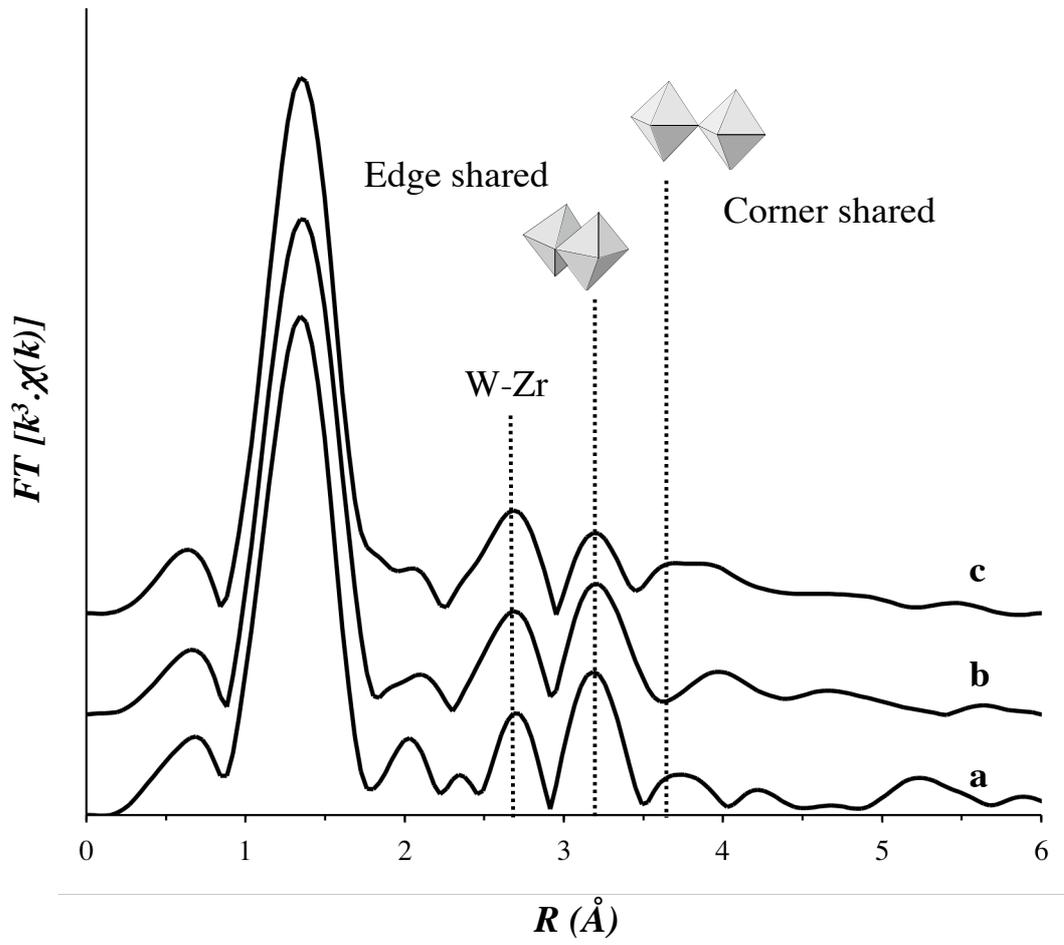**Figure 2**
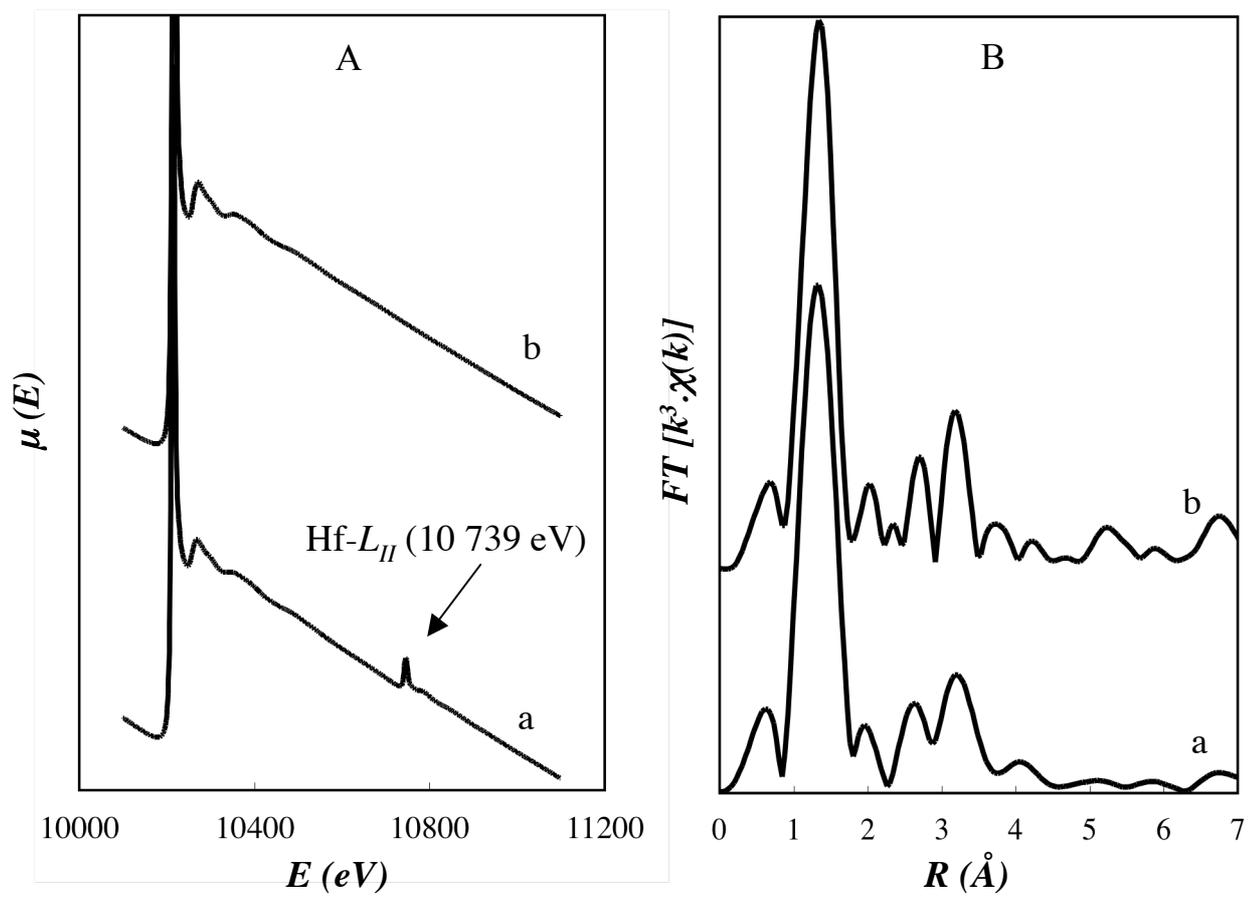
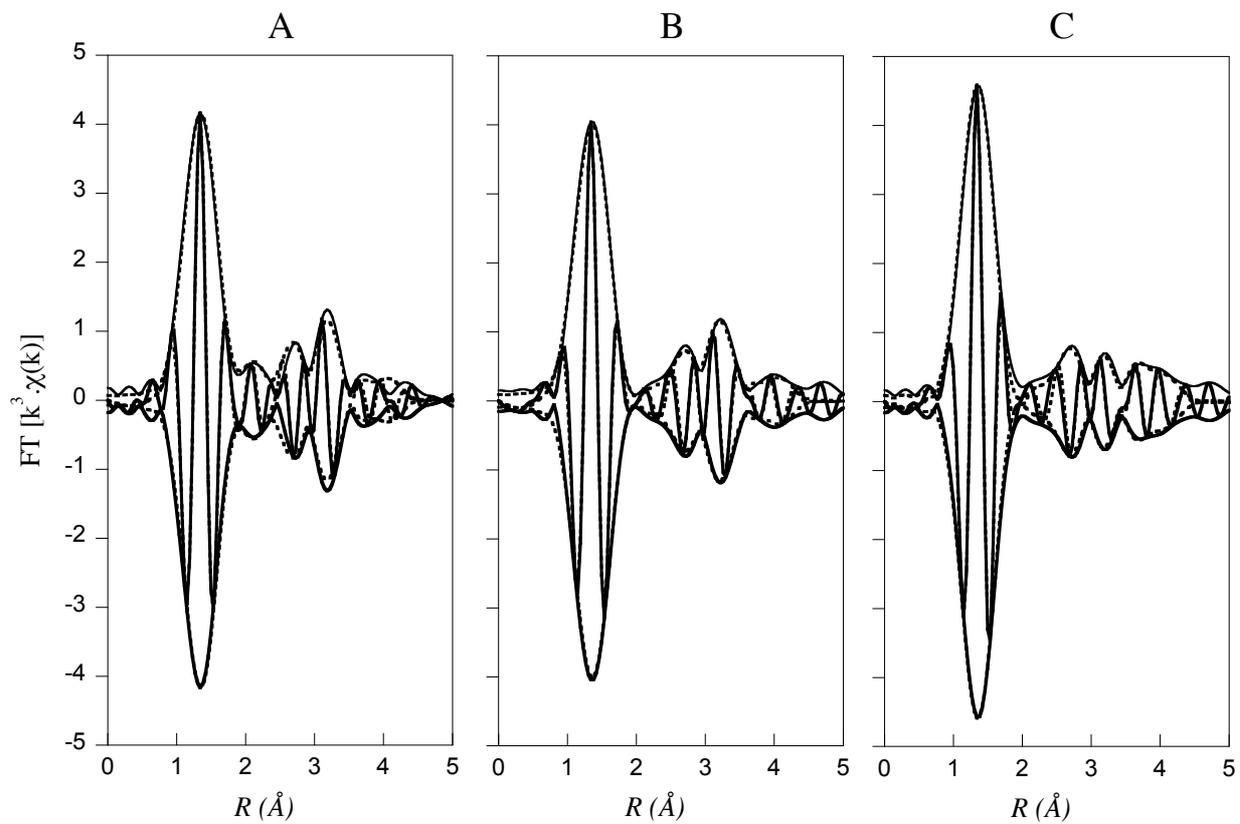**Figure 3**
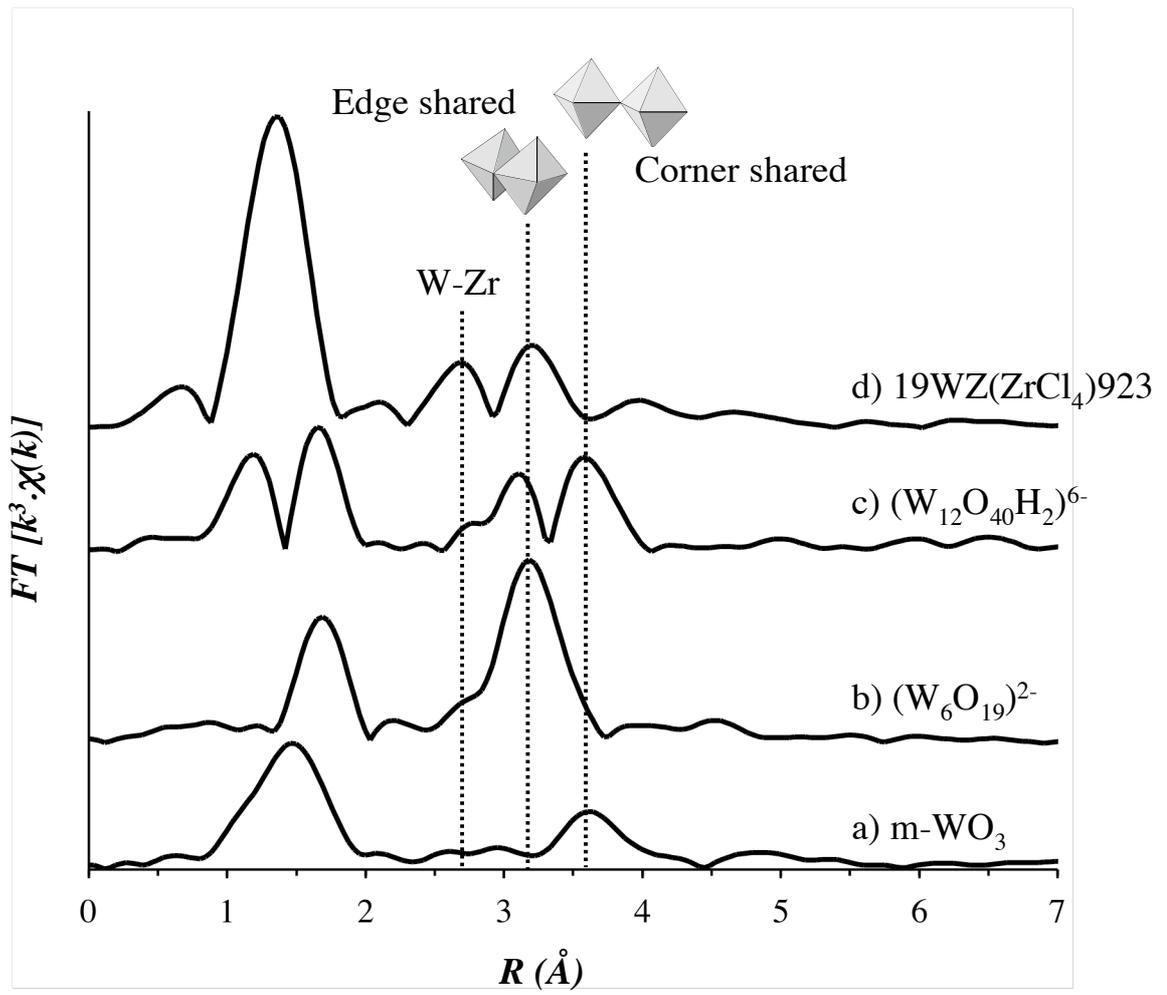
Figure 4

Figure 5

Figure 6

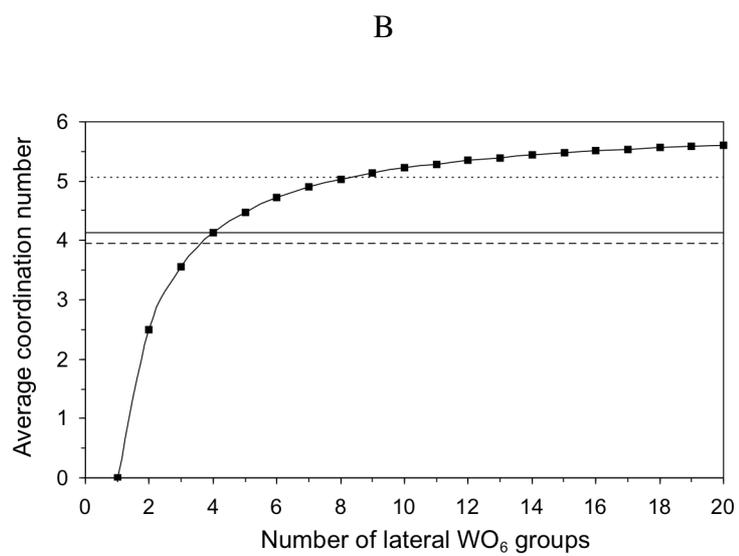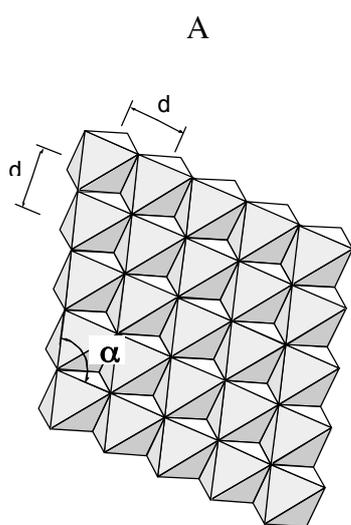A   B

Figure 7